

Title:

Improving the heat dissipation performance of a looped thermosyphon using low-GWP volatile fluids R1234ze(Z) and R1234ze(E) with a super-hydrophilic boiling surface

Authors:

Chieko KONDOU^{1,3*}, Shohei UMEMOTO¹, Shigeru KOYAMA^{2,3}, Yutaka MITOOKA⁴,

Affiliation:

¹ Graduate School of Engineering, Nagasaki University, 1-14 Bunkyo-machi Nagasaki 852-8521 Japan

² Interdisciplinary Graduate School of Engineering Sciences, Kyushu University, 6-1 Kasuga-koen, Kasuga, Fukuoka 816-8580, Japan

³ NEXT-RP in WPI-I²CNER, Kyushu University, 744 Motooka, Nishi-ku, Fukuoka 819-0395, Japan

⁴ Metal & Machining Group, Department of Research and Development, Industrial Technology Center of Okayama Prefecture, 5301 Haga Kita-ku, Okayama, 701-1296, Japan

* Corresponding author

Chieko Kondou, PhD

Associate Professor, Nagasaki University

Graduate School of Engineering, Division of System Science

1-14 Bunkyo-machi Nagasaki 852-8521 Japan

+81 95 819 2527 / ckondou@nagasaki-u.ac.jp

Abstract

With the rapid development of electronic devices, internal heat generation in these devices becomes significantly denser. Accordingly, their thermal management becomes increasingly important for stable operation. For the performance improvement of heat dissipation in limited installation spaces, passive two-phase cooling technique using water is applied. Instead of water, using a more volatile substance as the working fluid is advantageous in many aspects. For instance, the higher volumetric capacity that is the product of vapor density and latent heat of vaporization allows compactness, while higher boiling heat transfer coefficient can extend the stable operation conditions under heavy loads of the electronic devices. In this study, a gravity-driven cooling circuit known as thermosyphon using refrigerants R134a, R1234ze(E), and R1234ze(Z) is experimentally investigated. The experimental thermosyphon successfully kept the heating block temperature simulating electronic devices below 80 °C at heat fluxes up to 1400, 1250, and 1110 kWm⁻² with R134a, R1234ze(E), and R1234ze(Z), respectively. Furthermore, using a super-hydrophilic boiling surface fabricated by laser irradiation, the heat flux was extended to 1600, 1400, and 130 kWm⁻², respectively. The experiment demonstrated that using the selected volatile fluids and super-hydrophilic surfaces could be a beneficial method for cooling electronic devices.

NOMENCLATURE

D	diameter	[m]	ξ	volumetric filling ratio	[-]
I	current	[A]			
Q	heat transfer rate	[W]	subscript		
R	thermal resistance	[KW ⁻¹]	HB	heating block	
T	temperature	[°C]	L	saturated liquid	
V	voltage	[V]	SC	subcool	
a	temperature diffusivity	[m ² s ⁻¹]	SH	superheat	
g	gravitational acceleration	[ms ⁻²]	TP	test boiling surface	
m	charge amount	[kg]	V	saturated vapor	
q	heat flux	[Wm ⁻²]	air	air	
u_L	liquid back velocity	[ms ⁻¹]	boil	boiling	
v_{air}	air facing velocity	[ms ⁻¹]	chip	CPU chip	
x	position	[m]	cond	condenser	
Δh	specific enthalpy	[Jkg ⁻¹]	cont	contact	
ΔH	capillary height	[m]	heater	heater	
α	heat transfer coefficient	[Wm ⁻² K ⁻¹]	loss	heat loss	
λ	thermal conductivity	[Wm ⁻¹ K ⁻¹]	shunt	shunt resistance	
θ	contact angle	[°]	srf	surface	
ρ	density	[kgm ⁻³]	sys	system	
σ	surface tension	[Nm ⁻¹]	total	total	

1. INTRODUCTION

With rapid advancements in electronic devices, such as IGBT modules and highly integrated computers, heat generation in CPU (central processing unit) is becoming increasingly denser. The CPU power consumption reduction has been truly committed. Nevertheless, the heat dissipation by an air cooling system is no longer sufficient for next generation electronic devices. Thus, thermal management becomes a serious issue for stable operation and reliability. For heat dissipation from such high heat flux devices, shifting the cooling method from natural or forced convection to methods using phase change has attracted attention. Among the two-phase cooling methods, with respect to a reduction in thermal resistance, immersion boiling would be the ultimate solution (e.g., Wroblewski and Joshi [1], El-Genk and Bostanci [2]; Tuma [3]). However, wiring CPU in the pool and handling liquid pool in the limited installation spaces is a big concern. As for more realistic solutions, the following two devices are now being applied: 1) Heat pipes pump working fluids typically by capillary wicking, sometimes by pressure oscillation and so on; 2) thermosyphons circulate fluids by gravity (e.g., Agostini and Agostini [4], Khodabandeh and Palm [5]). Thus, of course, thermosyphons are available only in situations where the condenser is placed above the evaporator. Instead, because of the higher fluid circulation rate, thermosyphons can provide greater capacity than heat pipes in general. It seems that most of the studies related to thermosyphons address water and HFEs (hydro fluoro ethers), which have normal boiling points above room temperature and thus evaporate normally at pressures below the atmospheric pressure.

Palm and Khodabandeh [6] numerically investigated the impact of working fluids on the heat dissipation performance of thermosyphons. They suggested the most important issue is choosing a fluid to reduce the thermal resistance of the evaporator in which the heat transfer area contacting the CPU is limited. To increase the boiling heat transfer coefficient, the use of more volatile fluids is a very attractive option. In the numerical study, they referred R32 and R134a as the high-pressure fluids. In addition, fouling and contamination of non-condensable gases are avoidable with these volatile working fluids, which are normally supplied in high purity and operate at higher pressures than the atmospheric pressure. Moreno et al. [7-8] investigated the boiling characteristics of volatile fluids R1234yf and R245fa on a microporous coating surface for thermosyphons. However, to the best of our knowledge, assessment results of the system performance have not been reported for those fluids.

The other important factor for the evaporator part is the boiling surface characteristics. A well-known enhancement technique “reentrant cavity”, used in low heat flux applications, is no longer beneficial under high heat flux conditions near the CHF (critical heat flux), since this structure could obstruct the ingress of liquid and emerging vapor. For use of such high heat flux conditions, micro or nano scale fabrication on plain surfaces has been vigorously investigated in the past two decades.

For instance, El-Genk and Ali [9] produced Cu micro-porous surface by the electrochemical deposition method and demonstrated a significant enhancement in both the HTC (heat transfer coefficient) and CHF for pool boiling. According

to experiments using FC-72 by Rainey and You [10], the presence of large embryonic bubble diameters produced by increased vapor entrapment in the micro structure primarily enhanced nucleate boiling on roughed surfaces throughout the boiling curve and increased the CHF, but reduced the overshoot of onset boiling. Using UV radiated TiO₂ sputtered surface, which is a photo induced super-hydrophilic surface, Takata et al. [11] demonstrated heat transfer enhancement in the nucleate boiling region and also the CHF for water. Forrest et al. [12] showed a quite opposite conclusion. From their experiment using water and a nanoparticle coated nickel wire with a diameter of 0.25 mm, it was indicated that the super-hydrophilicity rather decreased nucleate boiling HTC but increased the CHF. Using varied wettability surfaces, Phan et al. [13] found that the best nucleate boiling HTC was obtained at a water contact angle of either 0 ° or 90 °. Medium hydrophilicity exhibited much lower HTC because of a decrease in the bubble emission frequency and an increase in the bubble departure diameter. Near the solid, liquid, and vapor coexistence line beneath the bubbles, typically called the triple contact line, the liquid evaporation rate is significantly high. Thus, on super-hydrophilic surfaces, speedy liquid advancing on the line compensates the negative effects shown with medium hydrophilicity and enhances both the nucleate boiling HTC and CHF [13]. O’Hanley et al. [14] experimentally attempted to separate the effects of microporous and wettability on CHF enhancement for water. Their results showed that a porous hydrophilic surface exhibited 1.5 times higher CHF than a non-porous hydrophilic surface. Therefore, they determined that capillary wicking in hydrophilic pores was the mechanism responsible for the CHF enhancement. Although there are still controversies, the number of previous works indicates favorable influences of a super-hydrophilic microporous surface on nucleate boiling HTC and CHF. However, information of those effects is very limited for high-pressure volatile fluids. Because of a much smaller surface tension than water, those effects are of great interest for high-pressure fluids.

There are many ways to create super-hydrophilic microporous surfaces. The coating of nano-particles is the most popular method. Among the methods, the new technique LISS (Laser Interference Surface Structuring) can produce micropores and chemical treatment both at the same time and create super-hydrophilic surfaces at a certain laser radiation condition (e.g., Vorobyev and Guo [15]; Chen et al. [16]). By this direct fabrication of material surfaces, the concern of adhesion, which often occurs in coating processes, is avoided. This method requires only several seconds to fabricate an area of a few square centimeters. Further, using laser equipment already introduced in many production sites could reduce industrial barriers.

From the above introduction, the heat dissipation performance of a gravity-driven thermosyphon using volatile working fluids R134a, R1234ze(E), and R1234ze(Z) is experimentally evaluated in this study to confirm the advantages to water. First, a machined plain surface is tested as the boiling surface. Next, the super-hydrophilic surface fabricated by LISS is tested with those selected fluids to confirm the effects on nucleate boiling HTC and CHF.

2. EXPERIMENTAL METHOD

2.1 Experimental setup

Fig. 1 (a) shows the experimental setup to measure the heat dissipation performance. This apparatus is designed as a natural circulation loop motivated by gravitation without a fluid pump for energy conservation. This mainly consists of a heating

block (a), an evaporator having a test boiling surface (b), a sight glass (c), and a condenser (d) of microchannel heat exchanger with a hydraulic inner diameter of 0.89 as illustrated in Fig. 1 (a). The total internal volume is determined as $2.69 \times 10^{-4} \text{ m}^3$ by preliminary measurements with nitrogen gas and R134a gas. The evaporator, the vapor line, the condenser, and the liquid line account for approximately 34%, 5%, 56%, and 5% of the internal volume, respectively. The air flow rate to the condenser is controlled by the rotation speed of a fan (e) in the air duct. The air velocity is measured by a hot-wire flow meter at 30 points and correlated to the input voltage of fan motor with an uncertainty of $\pm 0.1 \text{ ms}^{-1}$. The liquid pressure at the condenser outlet is measured with a pressure transducer. Temperatures at the outlet of the evaporator and condenser are measured with K-type thermocouples. From the measured pressure, a saturation temperature is evaluated at the measured pressure. The thermophysical properties of the working fluids are calculated with REFPROP Ver. 9.1. [17].

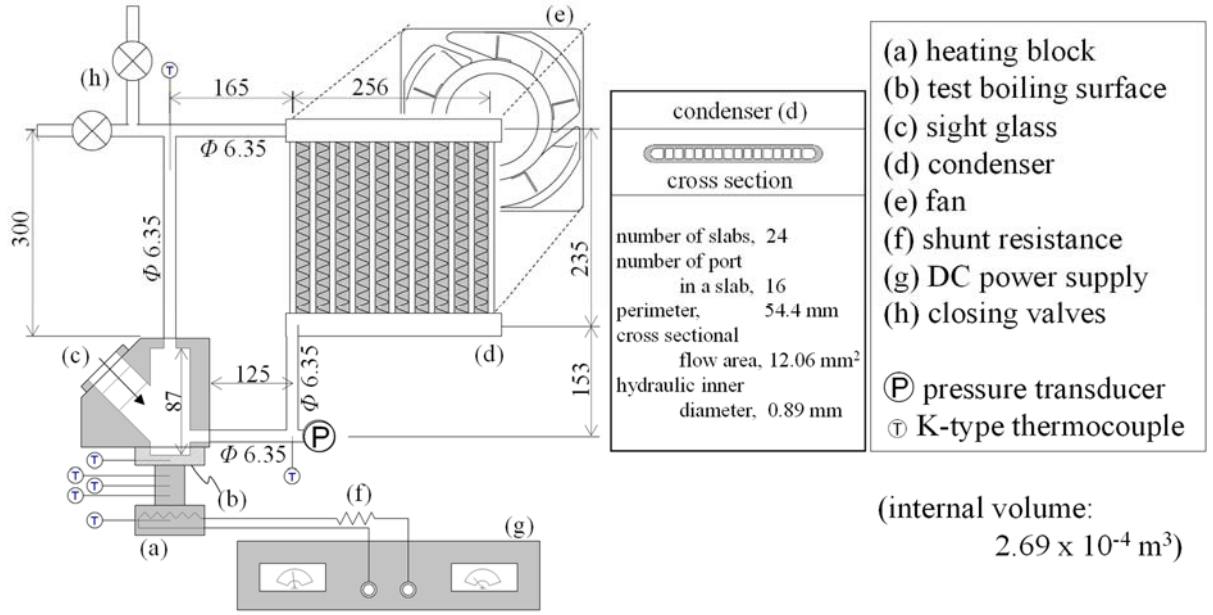
The heating block (a) made of oxygen free copper, which simulates a CPU chip, has two cartridge heaters, as shown in Fig. 1 (b). The heat generation rates of these cartridge heaters are determined by Ohm's law from the measured voltage drop over the cartridge heaters and the direct current measured at the shunt resistance (f) imposed by a DC power supply (g).

$$Q_{\text{heater}} = \sum (I_{\text{shunt}} V_{\text{heater}}) \quad (1)$$

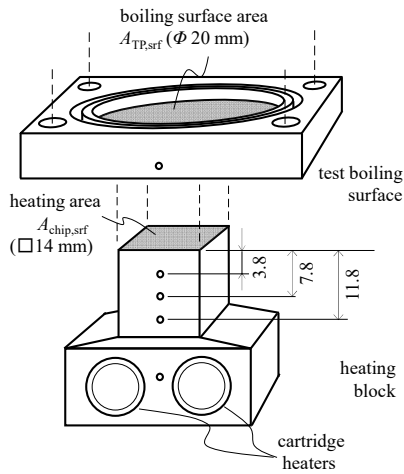
The heat flux q_{chip} from the heating block is determined as

$$q_{\text{chip}} = -\lambda_{\text{HB}} \left(\frac{dT}{dx} \right)_{\text{HB}} = \frac{Q_{\text{heater}} - Q_{\text{loss}}}{A_{\text{chip,srf}}} \quad (2)$$

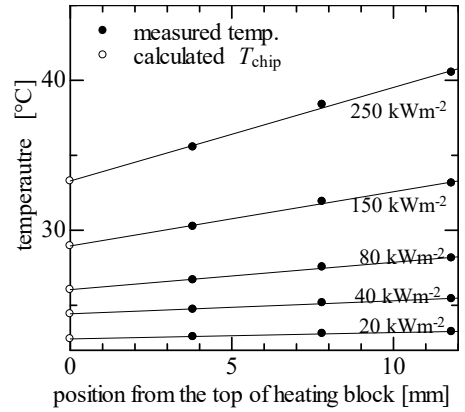
where λ_{HB} is the thermal conductivity of the heating block. $(dT/dx)_{\text{HB}}$ is the temperature gradient in the heating block. This is obtained from the measured temperatures at positions of 3.8 mm, 7.8 mm, and 11.8 mm from the top of the heating block, respectively, by the least square mean method as plotted in Fig. 1 (c). To ensure the validity of measurement method, it is confirmed that the heat loss to the ambient Q_{loss} is always positive value.



(a) test loop (unit; mm)



(b) heating block and test boiling surface



(c) procedure for determining T_{chip} and q_{chip}

Figure 1 Experimental setup

To evaluate the heat dissipation performance, thermal resistance quantified from the measured data are compared. The system thermal resistance, R_{sys} , is defined as:

$$R_{sys} = (T_{chip} - T_{air}) / (A_{chip,srf} q_{chip}) = R_{cond} + R_{boil} + R_{TP} + R_{cont}$$

$$\text{where, } \begin{cases} R_{cond} = (T_{sat} - T_{air}) / (A_{chip,srf} q_{chip}) \\ R_{boil} = (T_{TP,srf} - T_{sat}) / (A_{chip,srf} q_{chip}) \\ R_{TP} = (T_{TP,btm} - T_{TP,srf}) / (A_{chip,srf} q_{chip}) \\ R_{cont} = (T_{chip} - T_{TP,btm}) / (A_{chip,srf} q_{chip}) = 0.0714 \text{ [KW}^{-1}\text{]} \end{cases} \quad (3)$$

where T_{chip} is the surface temperature of the heating block and represents the chip (CPU) surface temperature. This is extrapolated from the measured temperature profile in the heating block, as shown in Fig. 1 (c). T_{air} is the ambient air temperature of 20 °C, which is kept constant in the entire experimental range. T_{sat} is the saturation temperature calculated from the measured pressure at the outlet of condenser. R_{cond} , R_{boil} , R_{TP} , and R_{cont} are thermal resistances of the condenser, the boiling heat transfer, heat conduction in the test boiling surface, and contact between the test boiling surface and the heating block, respectively. A small amount of thermal grease was applied on the contact surface between the test boiling surface and the heating block, and then they were fastened by screws. The contact thermal resistance R_{cont} ranged from 0.026 to 0.092 KW⁻¹ in the experiment. Reproducing exactly the same contact condition was difficult; therefore, the experimental data are reduced with an average value of 0.0714 KW⁻¹ to determine the total thermal resistance R_{sys} and chip temperature T_{chip} .

The volumetric filling ratio of working fluids, ξ , is obtained without heat load at ambient temperature, i.e., rest condition:

$$\xi = \frac{V_{\text{L}}}{V_{\text{total}}}, \quad V_{\text{L}} = \frac{m - \rho_{\text{V}} V_{\text{total}}}{\rho_{\text{L}} - \rho_{\text{V}}}, \quad (4)$$

where V_{total} , V_{liq} , and V_{vap} are the total, liquid, and vapor volumes of charged working fluids at the rest condition, respectively. ρ_{vap} and ρ_{liq} are densities of the saturated vapor and liquid evaluated at ambient temperature with REFPROP Ver. 9.1. m is the measured mass of charged working fluid. As expressed in the above equation, the charge amount of fluids is volumetrically evaluated with ξ at the rest condition.

2.2 Test fluids

Table 1 lists the test conditions and thermophysical properties of the tested fluids. The experimental data are taken with bare, super-hydrophilic, and sandblast surfaces at facing air velocities from 0.5 ms⁻¹ to 4.0 ms⁻¹, filling ratios ξ from 25% to 60%, and heat fluxes from 20 kWm⁻² to 1500 kWm⁻², for water, R134a, R1234ze(E), and R1234ze(Z). The ambient air temperature is kept at 20 °C in the entire experimental range.

Table 1 Test conditions and fluid information

working fluid	water	R134a CH ₂ FCF ₂	R1234ze(E) Trans-C ₂ F ₃ H=CHF	R1234ze(Z) Cis-C ₂ F ₃ H=CHF
boiling surface	bare	bare, super-hydrophilic	bare, super-hydrophilic, sandblast	bare, super-hydrophilic
filling ratio, ζ [%]			25 ~ 60	
facing air velocity, v_{air} [m s ⁻¹]			0.5 ~ 4.0	
heat flux, q_{chip} [kWm ⁻²]			20 ~ 1500	
ambient temperature, T_{air} [°C]			20	
GWP ₁₀₀ [18]	-	1300	< 1	< 1
pressure [MPa]	0.005 ~ 0.01	0.55 ~ 0.79	0.16 ~ 0.20	0.42 ~ 0.54
critical pressure [MPa]	22.06	4.06	3.63	3.53
critical temperature [°C]	373.95	101.06	109.36	150.12
surface tension [mN m ⁻¹]	71.2 (at 30 °C)	7.4 (at 30 °C)	8.2 (at 30 °C)	12.2 (at 30 °C)
latent heat of vaporization [kJ mg ⁻¹]	2430 (at 30 °C)	173 (at 30 °C)	163 (at 30 °C)	203 (at 30 °C)
density (liquid/vapor) [kg m ⁻³]	0.03 / 996 (at 30 °C)	38 / 1187 (at 30 °C)	31 / 1146 (at 30 °C)	10 / 1208 (at 30 °C)
liquid viscosity [mPa·s]	0.80	0.18	0.19	0.28

2.3 Test boiling surfaces

Fig. 2 shows photographs of the test boiling surfaces: bare surface, super-hydrophilic surface, and sandblast surface. These are made of oxygen free copper. The bare surface, shown in Fig. 2 (a), is a plain boiling surface which is quickly polished after the machining process. The super-hydrophilic surface, shown in Fig. 2 (b), is a plain surface fabricated by short-pulse laser irradiation with a wavelength of 532 nm. This technique, sometimes called “LISS (Laser Interference Surface Structuring)”, controls wetting phenomena with both surface topography and chemistry (e.g., Hans et al. [19], Ta et al. [20]). The laser irradiation conditions, such as power and frequency, are specified in the Appendix. As shown in Fig. 2 (b), the copper surface completely loses light reflection after the laser irradiation. The sandblast surface, shown in Fig. 2 (c), is a plain surface roughed by a sandblast. This surface loses luster although it still has light reflection.

Figs. 3 (a) and 3 (b) are photographs of droplets of pure (i.e., distilled) water (0.05 ml) on bare and super-hydrophilic surfaces to measure the contact angle. It should be noted that the surface tension of water is approximately 59 mNm⁻¹ at a pressure of 0.1 MPa. Fig. 3 (c) and 3 (d) show droplets of ethanol on bare and super-hydrophilic surfaces to measure the contact angle. The super-hydrophilic surfaces shows higher wettability with ethanol having surface tension of approximately 17 mNm⁻¹, which is closer to that of R1234ze(Z).

Figs. 4 (a), 4 (b), and 4 (c) are SEM images and a microscopic picture to show the textures of the bare and super-hydrophilic surfaces. As shown in Fig. 4(c), line-patterned valleys are periodically generated by the intensive photo-thermal energy irradiation which melts the surface material away from the high temperature spots. According to Hans et al. [19], LISS also induces an oxide layer of nano-meter thickness on the surface. This oxide layer, i.e., CuO, which is roughened by dense lamellae as shown in Fig. 4(b), plays a role to increase wettability. Identical roles of oxide lamellar layers in super-hydrophilicity were reported by Lee et al. [21] for aluminum, Guan et al. [22] for stainless steel, and Vorobyev and Guo [23] for silicon.

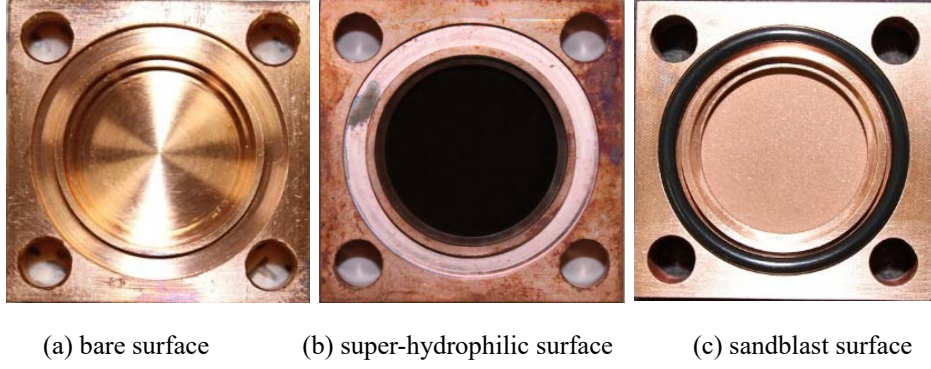


Figure 2 The test boiling surfaces (boiling surface area $A_{TP,srf}$ with a diameter of 200 mm)

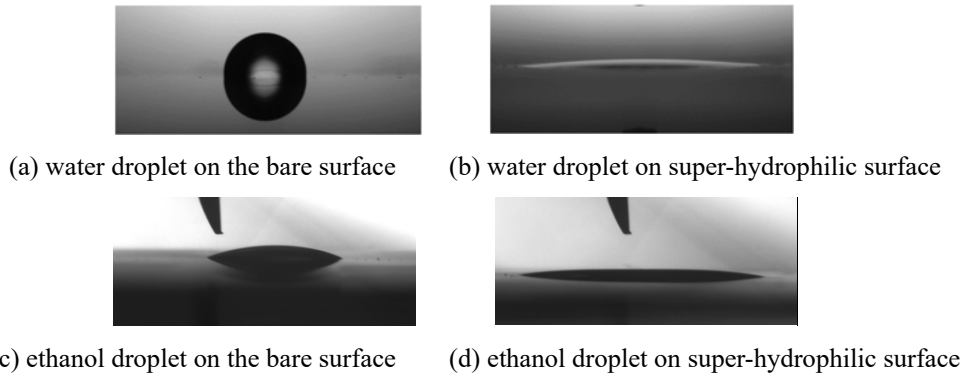


Figure 3 Contact angles with pure water and ethanol droplets with a volume of 0.05 ml

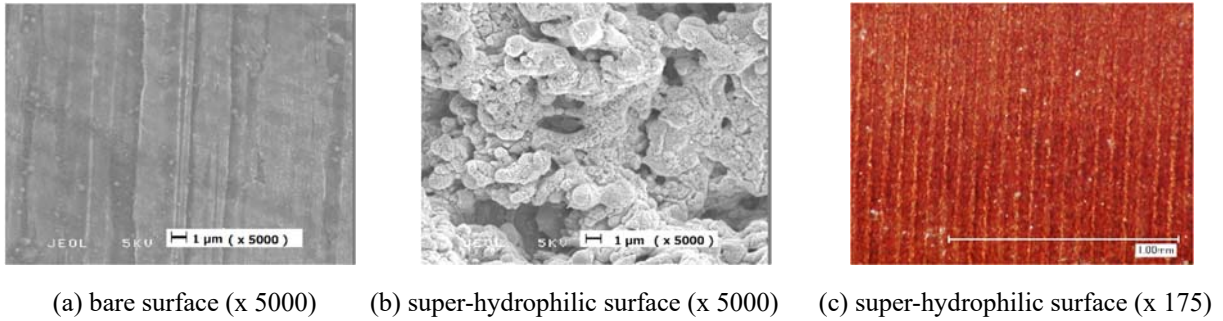


Figure 4 SEM images and a microscopic picture of the test boiling surfaces

Table 2 lists the specifications of the heating block and the test boiling surfaces. The heating area $A_{chip, srf}$, which is the contact area of the test boiling surfaces and the heating block simulating CPU chips, is 196 mm^2 . The boiling surface area $A_{TP,srf}$ is 314 mm^2 ; thus, the heat transfer area enlargement of the boiling surface to the heating area is 1.6. As listed in Table 2, the arithmetic mean surface roughness values of the bare, super-hydrophilic, and sandblast surfaces are $0.07 \mu\text{m}$, $0.93 \mu\text{m}$, and $3.52 \mu\text{m}$, respectively. The sandblast surface clearly exhibits a high roughness, whereas the super-hydrophilic surface exhibits slightly higher roughness relative to the bare surface because micron scale pits are made by laser irradiation, as shown in Fig. 4. The contact angles of 0.05 ml water droplets on bare and super-hydrophilic surfaces are 90.3° and 3.2° , respectively. The higher degree of oxidation due to excitation by high-energy exposure and the increased actual surface increase the wettability of metal surfaces [21-23]. The present data on the contact angles are in agreement with those of

copper.

Table 2 Specifications of the heating block and the test boiling surfaces

	bare	super-hydrophilic	sandblast
material	oxygen free copper (Cu > 99.6%)		
thickness [mm]	5.2		
boiling surface area, $A_{TP,srf}$ [mm ²]	314 (Φ 20)		
heating area (chip surface), $A_{chip,srf}$ [mm ²]	196 (14 x 14)		
arithmetic mean roughness [μ m]	0.07	0.93	3.52
contact angle with water [°]	90.3	3.2	-

3. RESULTS AND DISCUSSION

3.1 Effects of charge amount and air velocity on thermal resistances

Fig. 5 (a) plots the variation in total thermal resistance R_{sys} against the volumetric filling ratio ξ of R134a at a chip heat flux q_{chip} of 1000 kWm⁻² and a facing air velocity v_{air} of 2.5 ms⁻¹ for the cases of bare and super-hydrophilic surfaces. To show the factors influencing the R_{sys} variation, the thermal resistance by boiling heat transfer and that in the condenser, i.e., R_{boil} and R_{cond} , are plotted in Fig. 5 (b) for the case of the bare surface. At a smaller filling ratio, the system resistance is relatively higher due to higher boiling thermal resistance. This is attributed to a decrease in the liquid level accumulated in the evaporator with increasing heat flux, which is prone to cause dry-patch on the boiling surface. In contrast, at a larger filling ratio, plenty of liquid fills a portion of the condenser. This is typically called flooding and is represented by subcooling at the condenser outlet ΔT_{sc} , plotted in Fig. 5 (b). The flooding inactivates the heat transfer area in the condenser; thus, the system resistance increases with increasing condenser thermal resistance. As a consequence of the above, the optimum filling ratio, where the thermal resistance is minimized, is shown. The identical behavior of a thermosyphon using water with an internal volume of 43.2 cm³ was reported by Tsai et al. [24]. From a numerical simulation, Zhang et al. [25] showed that optimum performance occurred when the two-phase region area was maximum. The present data supported their observations. As shown in Fig. 5(a), the optimum filling ratio is approximately 40% for R134a. The apparent difference is not recognized between the bare and super-hydrophilic surfaces. Similarly, the optimum filling ratio is determined as 40% for R1234ze(E) and R1234ze(Z). However, for water, the ratio is determined as 60% in this study. That is notably larger than that of the other fluids. The difference is most likely caused by the disturbance of liquid return due to the notably higher capillary force of water. It seems that the notably large filling ratio is needed for water to avoid the dryout of evaporator due to the liquid retention in the condenser.

Fig. 6 shows the variation in the thermal resistances against facing air velocity for R134a at a heat flux of 1000 kWm^{-2} . As the facing air velocity increases, the air side heat transfer in the condenser increases. Thus, the total thermal resistance gradually decreases with decreasing condenser thermal resistance. Then, it plateaus at air velocities of more than 2.5 ms^{-1} . This is mainly due to plateaued air side heat transfer after the gradual transition from laminar to turbulent flow. To demonstrate the effects of the working fluid and boiling surface, the experimental data are hereafter compared at the facing air velocity of 2.5 ms^{-1} and the optimum filling ratio.

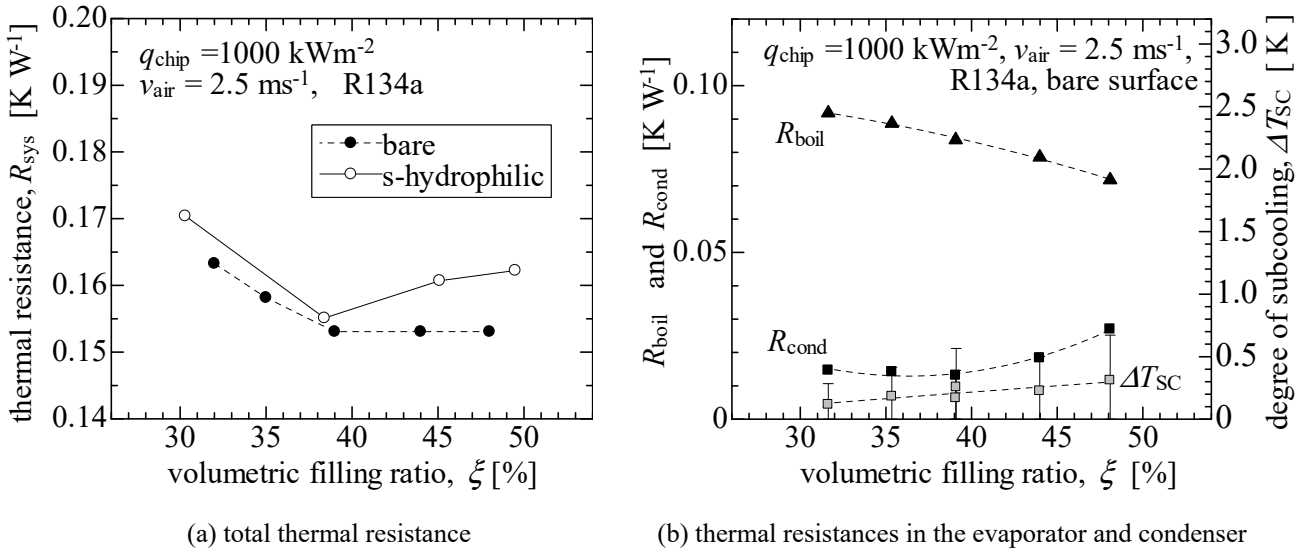


Fig. 5 Effect of volumetric filling ratio on thermal resistance

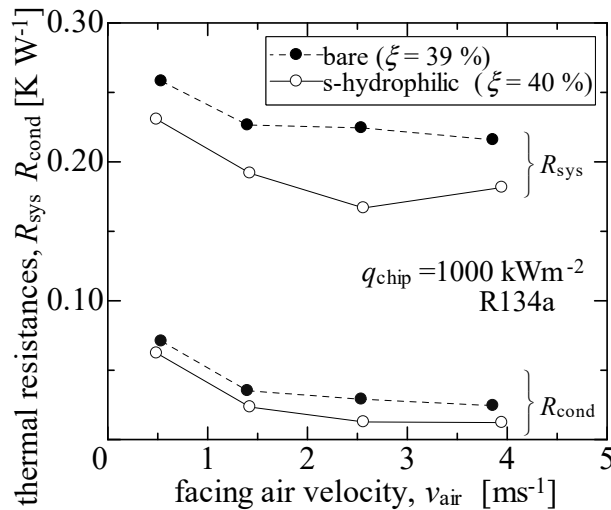


Fig. 6 Effect of facing air velocity on total thermal resistance

3.2 Effects of volatile working fluids

Fig. 7 plots the experimental data taken with the bare surface at a facing air velocity of 2.5 ms^{-1} and optimum filling ratios, as a function of heat flux and heat load. These include the data measured in the manner of increased and decreased heat flux, step-by-step. The vertical bars appended to the symbols of R_{sys} show the propagated measurement uncertainties of 95% coverage evaluated by the square-root rule [26-27].

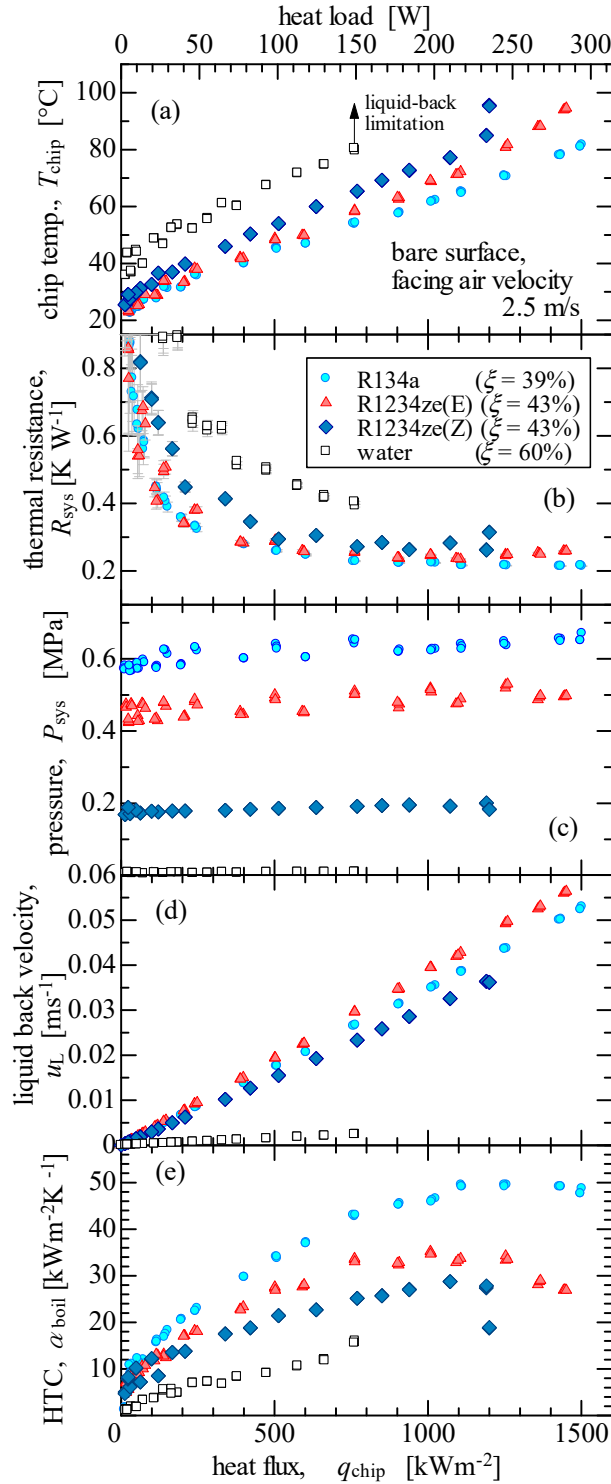


Figure 7 Effects of working fluids on heat dissipation performance.

Fig. 7 (a) shows the variation in the chip temperature, which is the top surface temperature of the heating block. The chip temperature T_{chip} increases almost proportionally with the chip heat flux q_{chip} , until it reaches a liquid-back limitation or a critical heat flux (CHF). Water exhibits obvious dryout, and drastic temperature increase on the boiling surface is encountered with insufficient liquid back at 750 kWm^{-2} . Assuming the contact angle θ with water is 45° and with the other test fluids is 5° , the capillary rise height

$$\Delta H = \frac{2\sigma \cos \theta}{\rho_L g (D/2)} \quad (5)$$

in a tube with an inner diameter D of 1 mm is calculated as 20 mm, 3.7 mm, 2.5 mm, and 2.1 mm for water, R1234ze(Z), R1234ze(E), and R134a, respectively. Liquid can be held in a narrow flow passage by the greater capillary force; therefore, the liquid-back limitation appears at a much lower heat flux for water. Upon further compactness, this issue would be a fatal problem for gravity-driven thermosyphons. With R1234ze(Z), a sudden temperature increase in T_{chip} is observed at 1180 kWm^{-2} ; however, liquid is still present in the evaporator. Thus, this sudden temperature rise is determined as the CHF.

Fig. 7 (b) shows the variation in the system thermal resistance. The system thermal resistance sharply decreases with increasing heat flux and then plateaus from this point on, where nucleate boiling with isolated bubbles fully develops. The system thermal resistance of water is notably higher than that of the others, and the system thermal resistance of R1234ze(Z) is somewhat higher than that of R1234ze(E) and R134a. The thermal resistance of R1234ze(E) is comparable to or slightly higher than that of R134a. Accordingly, the chip temperature reaches 80°C at heat fluxes of 750, 1100, 1250, and 1400 kWm^{-2} with water, R1234ze(Z), R1234ze(E), and R134a, respectively. The heat flux, where the CPU is kept below 80°C for stable operation, of water is notably lower than that of the others. Stable CPU operation could not be guaranteed with water at heat fluxes beyond 750 kWm^{-2} . The experiment demonstrates that refrigerants outperform water and notably extend the stable CPU operation range.

As plotted in Fig. 7 (c), the system pressures P_{sys} are determined as approximately 0.01 MPa, 0.2 MPa, 0.5 MPa, 0.6 MPa for water, R1234ze(Z), R1234ze(E), and R134a, respectively. Water exhibits a negative gauge pressure in all test conditions, which could cause contamination by the non-condensable gases. R1234ze(E) and R134a operate at somewhat higher pressures than R1234ze(Z). R1234ze(Z) operates at pressures closest to the atmosphere, which is a favorable condition for retrofitting.

Fig. 7 (d) shows the variation in the liquid back velocity u_L . The liquid back velocity u_L is the radially averaged velocity of liquid working fluid flowing in the downcomer, which is the pipe connects the condenser and the evaporator. The velocity u_L can be calculated as below.

$$u_L = \frac{(Q_{\text{heater}} - Q_{\text{loss}}) / (\Delta h_{\text{LV}} + \Delta h_{\text{SC}} |_{\Delta T_{\text{SC}}})}{\rho_{\text{SC}} (\pi D^2 / 4)} \quad (6)$$

The liquid enters the evaporator at this velocity and could provide additive convective effects on pool boiling heat transfer. Due to the much greater latent heat of water, the liquid back velocity is notably low for the other three working fluids. This could be another reason why the liquid-back limitation appears at a lower heat flux. Of the other working fluids, the liquid back velocity increases almost proportionally with increasing heat flux. This could help to enhance HTC and extend CHF.

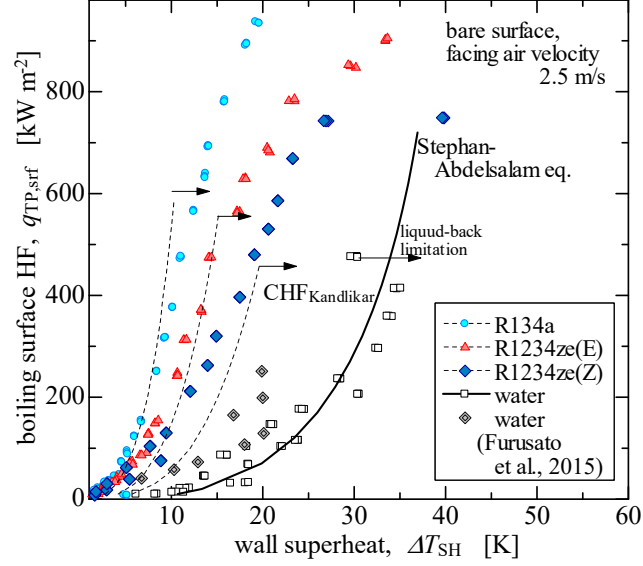


Fig. 8 Boiling curves and estimated CHF with bare surface

Fig. 8 compares the boiling curves with the bare surfaces among water, R1234ze(Z), R1234ze(E), and R134a. The vertical axis shows the average heat flux on the boiling surface with an area of $\phi = 20$ mm, i.e., 1/1.6 times of q_{chip} because of the area enlargement. As the heat flux increases, the superheat of test boiling surface, $\Delta T_{\text{SH}} = T_{\text{TP,srf}} - T_{\text{sat}}(P_{\text{sys}})$, increases. At a given heat flux, the wall superheats with refrigerants are considerably lower than with water. From this significant difference, the superior heat dissipation performance of refrigerants is attributed to the higher HTC of their nucleate boiling, which is also plotted in Fig. 7 (d).

The double-diamond symbols in Fig. 8 show the data obtained by Furusato et al. [28]. They examined the performance of a looped thermosiphon with water. Although their data show slightly smaller wall superheats because of the different system pressures, they satisfactorily agree with the present data of water. The solid and dashed curves in Fig. 8 show the following prediction of Stephan-Abdelsalam [29].

$$Nu = \frac{\alpha D_b}{\lambda_L} = 0.23 \left[\frac{q_{\text{TP,srf}} D_b}{\lambda_L (T_{\text{sat}} + 273.15)} \right]^{0.674} \left(\frac{\rho_V}{\rho_L} \right)^{0.297} \left(\frac{\Delta h_{\text{LV}} D_b}{a_L} \right)^{0.371} \left(\frac{\rho_L - \rho_V}{\rho_L} \right)^{-1.73} \left(\frac{a_L^2 \rho_L}{\sigma D_b} \right)^{0.35} \quad (7)$$

where, $D_b = 0.146 \beta \sqrt{\frac{2\sigma}{2g(\rho_L - \rho_V)}}$, $\beta = \begin{cases} 45^\circ & \text{for water} \\ 5^\circ & \text{for refrigerants} \end{cases}$

For the evaluation of thermophysical properties and saturation temperature in Eq. (7), the first-order approximation formula obtained from the experimental pressures plotted in Fig.7 (c) is used. The arrows at the end of the dashed curves show the

estimated CHF proposed by Kandlikar [30] and Zuber et al. [31] for pool boiling.

$$q_{\text{CHF}} = c_{\text{Zuber}} \times \Delta h_{\text{LV}} \rho_{\text{V}}^{1/2} \left(\frac{1 + \cos \beta}{16} \right) \left[\frac{2}{\pi} + \frac{\pi}{4} (1 + \cos \beta) \right]^{1/2} \left[\sigma g (\rho_{\text{L}} - \rho_{\text{V}}) \right]^{1/4} \quad (8)$$

$$c_{\text{Zuber}} = 1 + 5.30 \left(\frac{\rho_{\text{L}}}{\rho_{\text{V}}} \right)^{3/4} \left[\left(\frac{\rho_{\text{L}} \lambda_{\text{L}}}{\sigma} \right) / \sqrt{g (\rho_{\text{L}} - \rho_{\text{V}})} \right]^{1/4} \frac{C_{p_{\text{L}}} \Delta T_{\text{SC}}}{\Delta h_{\text{LV}}}$$

The CHF is evaluated by using a measured maximum pressure at a facing air velocity of 2.5 ms^{-1} those are 0.65 MPa, 0.51 MPa, 0.20 MPa, 0.012MPa for R134a, R1234ze(E), R1234ze(Z) and water, respectively.

Despite of the effects of liquid-back velocity and churning low liquid surface in the evaporator, the predicted boiling curves show better fit to the experimental data at heat fluxes below 500 kWm^{-2} . Conversely, the experimental CHF shows considerable extension from the estimated CHF of pool boiling. The CHF of R134a is out of the experimental range, which is restricted by a melting temperature ($200 \text{ }^{\circ}\text{C}$) of an alloy soldering the heating block and the cartridge heaters. However, the experimental data indicates much higher CHF than the predicted. The CHF of R1234ze(Z) is approximately 750 kWm^{-2} . At 900 kWm^{-2} , R1234ze(E) drastically increases in wall superheat, which indicates the bubble coalescence and is close to the CHF. These heat fluxes are 1.6 times the predicted pool boiling CHF. This significant discrepancy can be explained with the liquid-back velocity, which is more than 0.03 ms^{-1} at this condition, which is probably enough for blowing off the vapor bubbles and prompting surface rewetting. As mentioned, the smooth liquid-back of refrigerants is very effective for the CHF extension.

3. 3 Effects of super-hydrophilic surface fabricated by LISS

Figs. 9 (a), (b), and (c) compare the system thermal resistance and the chip temperature between the bare and super-hydrophilic surfaces for R1234ze(Z), R1234ze(E), and R134a, respectively. For those fluids, the super-hydrophilic surface exhibits somewhat lower chip temperature and system thermal resistance relative to the bare surface. By using the super-hydrophilic surface, the maximum heat flux where the chip temperature is kept below $80 \text{ }^{\circ}\text{C}$ is extended from 1100 to 1350 Wm^{-2} for R1234ze(Z), from 1250 to 1400 kWm^{-2} for R1234ze(E), from 1400 to 1600 kWm^{-2} for R134a. Thus, to extend the reliable CPU operation range, using a super-hydrophilic surface seems to be a promising idea for these working fluids. The effects of super-hydrophilicity are more evident for R1234ze(Z) which has a larger surface tension.

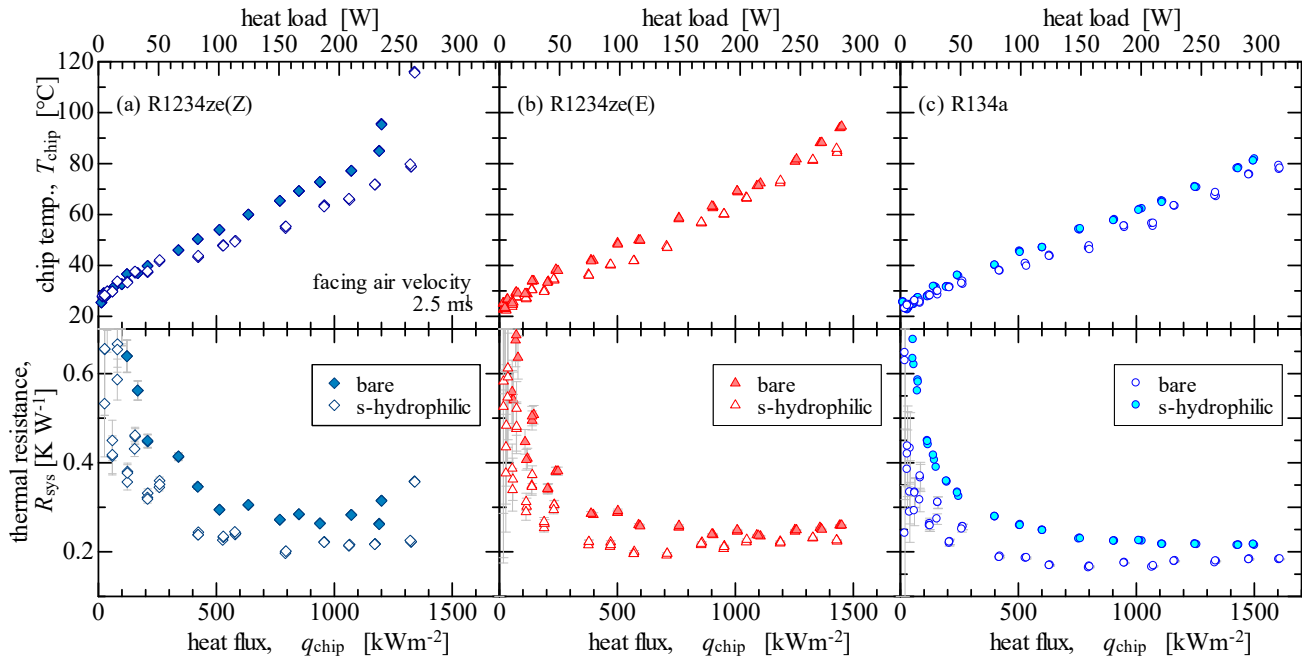


Fig. 9 Effects of super-hydrophilic surface on chip temperature and system thermal resistance

Fig. 10 plots the boiling curves for R1234ze(Z), R1234ze(E), and R134a to show the heat transfer enhancement by the super-hydrophilic surface fabricated by LISS. The solid and dashed lines show the data series taken at heat fluxes varied in incremental and decremental steps, respectively. The well-known hysteresis of nucleate boiling inception is observed with the super-hydrophilic surface at heat fluxes below 150 kW m^{-2} . At heat fluxes beyond 150 kW m^{-2} , the wall superheat is significantly decreased by using the super-hydrophilic surface for these selected working fluids. Similar effects in using a super-hydrophilic surface have been reported in numerous literature investigations mostly focused on water boiling at atmospheric pressure [11][32]. The surface tensions of R1234ze(Z), R1234ze(E), and R134a are 1/6, 1/9, and 1/10 of water, respectively. Although the surface tensions of these fluids are considerably small, the effects of the super-hydrophilic surface are identified.

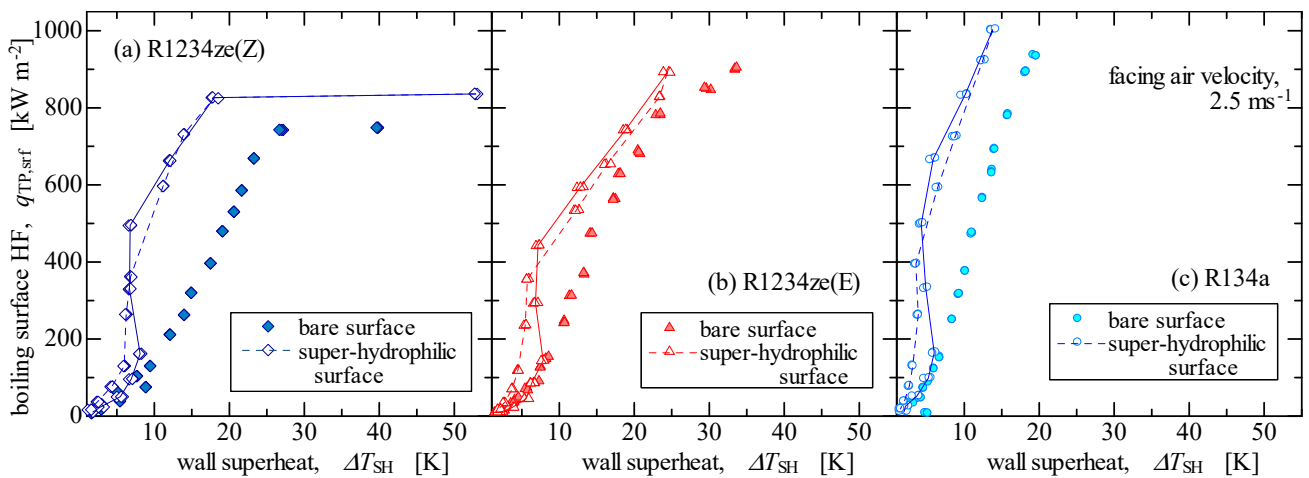


Fig. 10 Changes in the boiling curves by the super-hydrophilic surface

Fig. 11 compares the boiling curves among the bare, super-hydrophilic, and sand blast surfaces. The solid and dashed lines are the data series measured in incremental and decremental steps of heat flux, respectively. At heat fluxes above 150 kWm^{-2} where nucleate boiling develops, the super-hydrophilic and the blast surfaces both exhibit reductions in the wall superheat, and it is more evident for the super-hydrophilic surface. Comparing to the bare surface, the super-hydrophilic surface reduces the wall superheat by approximately 6 K; on the other hand, the blast surface reduces the wall superheat by approximately 3 K. Moreno et al. [7] tested the pool boiling of R1234yf, which has similar thermodynamic properties as R1234ze(E), with a copper microporous-coating surface. In their data, wall superheat is reduced by approximately 4 K by the coating at a heat flux of 300 kWm^{-2} . This is very similar to the trend of the present data of the sand blast surface. The super-hydrophilic surface still monotonically increases the wall superheat even at a heat flux of 900 kWm^{-2} which is close to the CHF of the bare surface. The super-hydrophilic surface seems to also enhance the CHF and prevent a sudden increase in the chip temperature. However, the boiling curve of the blast surface merges to that of the bare surface at a heat flux of approximately 700 kWm^{-2} . It appears that the blast surface has almost no effects on the CHF, although the blast surface has considerably higher roughness.

The tested super-hydrophilic surface fabricated by LISS is topographically and chemically characterized. The topographic feature mostly provides the effects of micropores (surface roughness); whereas the chemical feature (oxidation) provides the effects of wettability. From both features, strong wicking effects can be expected. This would cause the difference between the LISS super-hydrophilic surface and the sand blast surface.

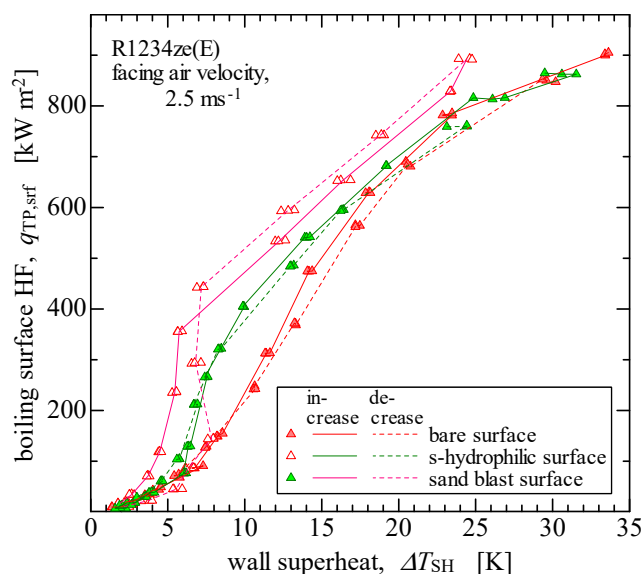


Fig. 11 Effects of the boiling surface on pool boiling heat transfer

By the visualization of pool boiling using HFE-7100, Thiagarajan et al. [33] demonstrated that a copper microporous coating enhanced nucleate HTC because of the much denser nucleation site on the roughed surfaces. From the experiment of pool boiling FC-72 on various micro surfaces at atmospheric pressure, Chang and You [34] attributed the mechanism of heat transfer enhancement on microporous surfaces to increased external vaporization, smaller departing bubble sizes, and higher bubble departure frequencies produced from the microporous structure. The findings of the present results seem to

be essentially identical to those above. However, those literature investigations remarked that the enhancement was observed on the entire boiling surface and that CHF was also enhanced. This discrepancy could be produced by the structural difference of the micropores, adhesive strength of coating, or wettability. Unfortunately, the detailed information is insufficient to deduce the factors. With deionized water, Rahman et al. [35] experimentally determined that wickability was the single factor of CHF enhancement using super-hydrophilic surfaces. O'Hanley et al. [14] experimentally separated the effects of micropores and wettability and concluded that capillary wicking produced by micropores and wettability were both the mechanisms responsible for the CHF enhancement. The latter two studies support the difference found between the LISS super-hydrophilic surface and blast surface.

Fig. 12 shows a breakdown of the thermal resistance for the tested combination at a heat flux of 750 kW m^{-2} and an air velocity of 2.5 ms^{-1} . The combination of water and bare surface is notably higher than the others and thermal resistance by boiling R_{boil} dominates the system thermal resistance. By introducing the volatile working fluids, R_{boil} is markedly reduced. By using the super-hydrophilic surface, R_{boil} is reduced furthermore. The thermal resistance of condenser R_{cond} ranges from 0.01 to 0.04, which is much smaller than R_{boil} because the condenser heat transfer area is significantly larger as compared with the boiling surface area. The heat conduction thermal resistance through the test boiling surface R_{TP} depends on the thickness and thermal conductivity. Thus, it is always 0.06 KW^{-1} . The contact thermal resistance is assumed as 0.0714 KW^{-1} . These two thermal resistances are no longer negligible in the advanced combination using the volatile working fluids and the super-hydrophilic surface.

Considering the impact on global warming, R134a should be substituted for low GWP substances R1234ze(E) and R1234ze(Z), which exhibits almost comparable heat dissipation performance. With the super-hydrophilic surface, the performance of R1234ze(Z) is comparable to that of R1234ze(E) in the nucleate boiling region. Thus, R1234ze(Z), which operates closer to the atmospheric pressure, could be an attractive option for easier retrofitting to existing thermosiphon devices.

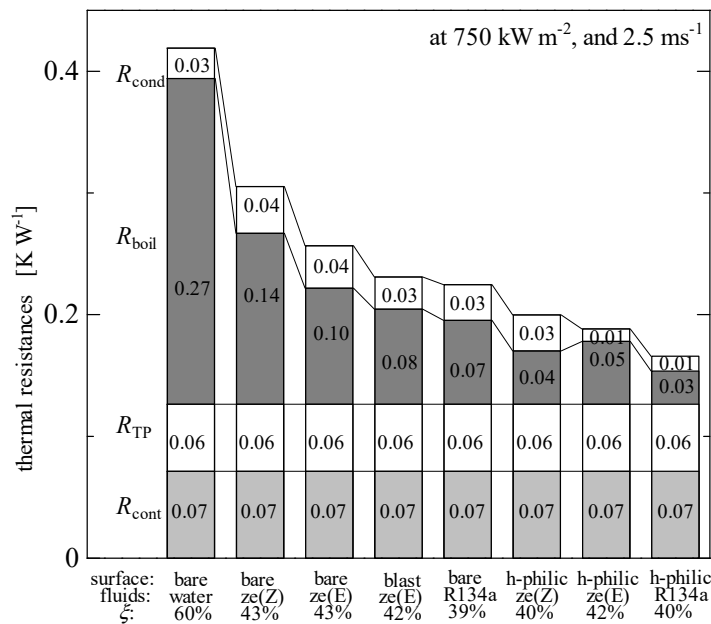


Fig. 12 Breakdown of thermal resistance for tested combinations.

4. CONCLUSIONS

Boiling heat dissipation experiments were conducted with a natural circulation loop to characterize the performance of working fluids: water, R1234ze(Z), R1234ze(E), and R134a. Additionally, the boiling surface, bare surface, and super-hydrophilic surface fabricated by LISS (Laser Interference Surface Structuring) were tested with those fluids to confirm enhancements in the nucleate boiling HTC (heat transfer coefficient) and the CHF (critical heat flux).

The experiment demonstrated that the selected volatile working fluids achieved superior heat dissipation performance compared to water due to their higher boiling HTC, which can significantly extend the stable CPU operation range. Additionally, the liquid-back limitation, which was present when using water, was resolved with the volatile fluids for chip heat flux up to 1500 kWm^{-2} . This finding was attributed to smaller capillary effects due to their smaller surface tensions and higher liquid-back velocities. This smooth liquid-back effectively extended the CHF. The system using R1234ze(E) exhibited almost comparable performance as R134a, while slightly outperforming R1234ze(Z).

Furthermore, the LISS super-hydrophilic surface improved the heat dissipation performance of the system using the above volatile fluids. Although the surface tensions of these fluids were considerably smaller than that of water, enhancements in the nucleate boiling heat transfer and CHF were identified by the experiments. The enhancement in the nucleate boiling HTC by the super-hydrophilic surface was more evident with R1234ze(Z), which has a somewhat greater surface tension than R1234ze(E).

Considering the environmental impact, R134a with high GWP should be alternated with R1234ze(E) or R1234ze(Z) as the potential working fluids of a thermosyphon. With the super-hydrophilic surface, R1234ze(Z), which operates closer to the atmospheric pressure, could be an attractive option for retrofitting.

APPENDICES

A. Laser irradiation condition

The laser irradiation conditions for LISS (Laser Interference Surface Structuring) are described here. For the fabrication of oxygen free copper surface, a Q-switch pulse YAG laser (Amadamiyachi ML-9001A) with a wavelength of 532 nm (SHG) is employed. The beam spot is approximately $50 \mu\text{m}$ at the maximum. With a single path, the beam quality is maximum 1.5. The repetition frequency, scanning speed and pitch of scanning arrays are varied from 1 to 20 kHz; from 100 to 500 mms^{-1} ; 10 and 30 μm , respectively, under atmospheric condition. The contact angle with a 0.05 ml pure water droplet is plotted as a function of repetition frequency in Fig. A. From this figure, the condition of 20 kHz frequency, 100 mm^{-1} scanning speed, and 30 μm pitch is selected for the boiling test. Additionally, it is confirmed that the water contact angle on the sample fabricated with the selected condition does not change after 1 hour of heating in a furnace at $100 \text{ }^\circ\text{C}$.

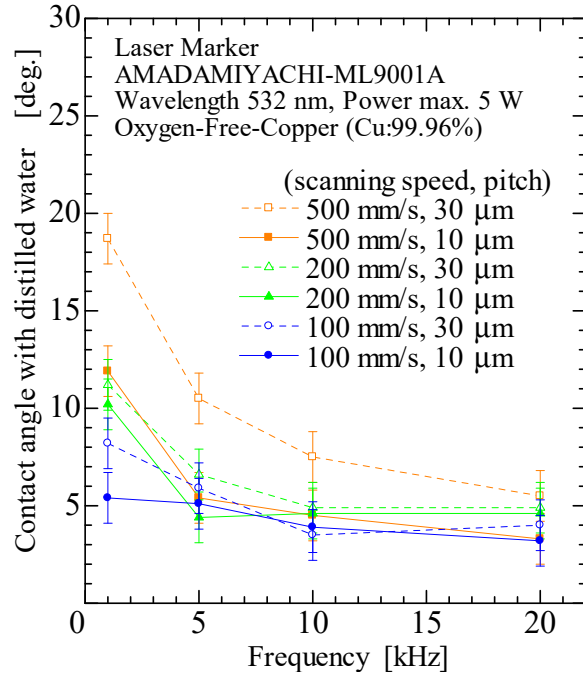


Fig. A Variation in water contact angle against laser irradiation conditions

B. Uncertainty Analysis

Table B1 lists the measurement uncertainty for each parameter. The 95% coverage of the uncertainty propagated with those variables are calculated by means of the square-root rule [26-27]), assuming that the variables are independent and their uncertainties are random. The calculation procedures are stated below.

Table B1 Measurement uncertainties

measured values	instrument	uncertainty
temperature in the heating block, T_1, T_2, T_3	thermocouples	± 0.05 K
temperature in the test boiling surface, T_{TP}		
ambient temperature, T_{air}	thermocouples	± 0.14 K
position in the heating block, x_1, x_2, x_3	slide caliper	± 0.01 mm
position in the test boiling surface, x_4, x_5		
facing air temperature, T_{air}	thermocouples	± 0.14 K
pressure, P	absolute pressure transducer	± 0.5 kPa (± 0.02 kPa for water)
thermal conductivity, $\lambda_{TP}, \lambda_{HB}$	-	± 2 $\text{Wm}^{-1}\text{K}^{-1}$

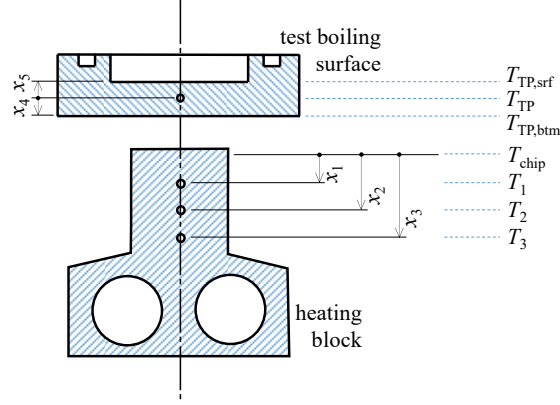


Fig. B1 Temperature measurement positions

B.1 Uncertainty in heat flux q_{chip}

The temperature gradient in heating block is obtained from three temperatures, T_1 , T_2 , and T_3 , at positions of x_1 , x_2 and x_3 as shown in Fig. B1. For instance, the temperature gradient between x_1 and x_2 can be obtained as,

$$\left(\frac{dT}{dx}\right)_{1-2} = \frac{(T_2 - T_1)}{(x_2 - x_1)}. \quad (\text{B1})$$

Thus, the uncertainty in $(dT/dx)_{1-2}$ is,

$$U_{(dT/dx)_{1-2}}^2 = \left(-\frac{1}{x_2 - x_1} U_{T_1}\right)^2 + \left(\frac{1}{x_2 - x_1} U_{T_2}\right)^2 + \left[-\frac{T_2 - T_1}{(x_2 - x_1)^2} U_{x_1}\right]^2 + \left[\frac{T_2 - T_1}{(x_2 - x_1)^2} U_{x_2}\right]^2. \quad (\text{B2})$$

Similarly, the temperature gradient $(dT/dx)_{2-3}$ and $(dT/dx)_{1-3}$, and their uncertainties are obtained. From those, the average temperature gradient and its uncertainty are calculated as below.

$$\left(\frac{dT}{dx}\right)_{\text{HB}} = \frac{1}{3} \left[\left(\frac{dT}{dx}\right)_{1-2} + \left(\frac{dT}{dx}\right)_{2-3} + \left(\frac{dT}{dx}\right)_{1-3} \right] \quad (\text{B3})$$

$$U_{(dT/dx)_{\text{HB}}}^2 = \left(\frac{1}{3} U_{(dT/dx)_{1-2}}\right)^2 + \left(\frac{1}{3} U_{(dT/dx)_{2-3}}\right)^2 + \left(\frac{1}{3} U_{(dT/dx)_{1-3}}\right)^2 \quad (\text{B4})$$

Lastly, the uncertainty in heat flux from the heating block, q_{chip} , calculated as Eq. (2) is estimated by the following equation.

$$U_{q_{\text{chip}}}^2 = \left[-\left(\frac{dT}{dx}\right)_{\text{HB}} U_{\lambda_{\text{HB}}} \right]^2 + \left(-\lambda_{\text{HB}} U_{(dT/dx)_{\text{HB}}} \right)^2. \quad (\text{B5})$$

B.2 Uncertainty in temperatures T_{chip} , $T_{\text{TP,btm}}$, $T_{\text{TP,srf}}$, and T_{sat}

The chip temperature can be determined from the temperature gradient $(dT/dx)_{\text{HB}}$ and the measured three temperatures T_1 , T_2 , and T_3 .

$$T_{\text{chip}} = \frac{1}{3} \left\{ \left[T_1 - \left(\frac{dT}{dx} \right)_{\text{HB}} x_1 \right] + \left[T_2 - \left(\frac{dT}{dx} \right)_{\text{HB}} x_2 \right] + \left[T_3 - \left(\frac{dT}{dx} \right)_{\text{HB}} x_3 \right] \right\} \quad (\text{B6})$$

The uncertainty in the chip temperature determined from the temperature T_1 is,

$$U_{T_{\text{chip},1}}^2 = U_{T_1}^2 + \left[- \left(\frac{dT}{dx} \right)_{\text{HB}} U_{x_1} \right]^2 + \left(x_1 U_{(dT/dx)_{\text{HB}}} \right)^2 \quad (\text{B7})$$

The uncertainties in $T_{\text{chip},2}$ and $T_{\text{chip},3}$, which are the chip temperature determined from T_2 and T_3 , are calculated in the same way. Thus, the uncertainty in chip temperature is estimated as following.

$$U_{T_{\text{chip}}}^2 = \left(\frac{U_{T_{\text{chip},1}}}{3} \right)^2 + \left(\frac{U_{T_{\text{chip},2}}}{3} \right)^2 + \left(\frac{U_{T_{\text{chip},3}}}{3} \right)^2 \quad (\text{B8})$$

The temperatures at the bottom and the upper surface of the boiling test surface are obtained from the measured temperature T_{TP} as shown in Fig. B1.

$$T_{\text{TP,btm}} = T_{\text{TP}} + \frac{1}{\lambda_{\text{TP}}} \int_0^{x_4} q_{\text{TP}} dx \quad (\text{B9})$$

$$T_{\text{TP,srf}} = T_{\text{TP}} - \frac{1}{\lambda_{\text{TP}}} \int_0^{x_5} q_{\text{TP}} dx \quad (\text{B10})$$

The uncertainties of those temperature are estimated by the following equations.

$$U_{T_{\text{TP,btm}}}^2 = \left(U_{T_{\text{TP}}} \right)^2 + \left(\frac{x_4}{\lambda_{\text{TP}}} U_{q_{\text{TP}}} \right)^2 + \left(\frac{q_{\text{TP}}}{\lambda_{\text{TP}}} U_{x_4} \right)^2 + \left(\frac{q_{\text{TP}} x_4}{\lambda_{\text{TP}}^2} U_{\lambda_{\text{TP}}} \right)^2 \quad (\text{B11})$$

$$U_{T_{\text{TP,srf}}}^2 = \left(U_{T_{\text{TP}}} \right)^2 + \left(- \frac{x_5}{\lambda_{\text{TP}}} U_{q_{\text{TP}}} \right)^2 + \left(- \frac{q_{\text{TP}}}{\lambda_{\text{TP}}} U_{x_5} \right)^2 + \left(\frac{q_{\text{TP}} x_5}{\lambda_{\text{TP}}^2} U_{\lambda_{\text{TP}}} \right)^2 \quad (\text{B12})$$

The uncertainty in the saturation temperature T_{sat} depends on the working fluids and the pressure measured by the absolute pressure transducer. That is calculated by using REFPROP 9.1.

$$U_{T_{\text{sat}}} = f_{\text{Refprop9.1}}(P \pm U_P) \quad (\text{B13})$$

B.2 Uncertainty in thermal resistances R_{cont} , R_{TP} , R_{boil} , R_{cond} , and R_{sys}

The thermal resistances are defined as Eq. (3) in this study. Therefore, the uncertainties in R_{cont} , R_{TP} , R_{boil} , and R_{cond} , can be estimated by the following equations.

$$U_{R_{\text{cont}}}^2 = \left(\frac{1}{A_{\text{chip,srf}} q_{\text{chip}}} U_{T_{\text{chip}}} \right)^2 + \left(\frac{-1}{A_{\text{chip,srf}} q_{\text{chip}}} U_{T_{\text{TP,btm}}} \right)^2 + \left[-\frac{T_{\text{chip}} - T_{\text{TP,btm}}}{(A_{\text{chip,srf}} q_{\text{chip}})^2} U_{A_{\text{chip,srf}} q_{\text{chip}}} \right]^2 \quad (\text{B14})$$

$$U_{R_{\text{TP}}}^2 = \left(\frac{1}{A_{\text{chip,srf}} q_{\text{chip}}} U_{T_{\text{TP,btm}}} \right)^2 + \left(\frac{-1}{A_{\text{chip,srf}} q_{\text{chip}}} U_{T_{\text{TP,srf}}} \right)^2 + \left[-\frac{T_{\text{TP,btm}} - T_{\text{TP,srf}}}{(A_{\text{chip,srf}} q_{\text{chip}})^2} U_{A_{\text{chip,srf}} q_{\text{chip}}} \right]^2 \quad (\text{B15})$$

$$U_{R_{\text{boil}}}^2 = \left(\frac{1}{A_{\text{chip,srf}} q_{\text{chip}}} U_{T_{\text{TP,srf}}} \right)^2 + \left(\frac{-1}{A_{\text{chip,srf}} q_{\text{chip}}} U_{T_{\text{sat}}} \right)^2 + \left[-\frac{T_{\text{TP,srf}} - T_{\text{sat}}}{(A_{\text{chip,srf}} q_{\text{chip}})^2} U_{A_{\text{chip,srf}} q_{\text{chip}}} \right]^2 \quad (\text{B16})$$

$$U_{R_{\text{cond}}}^2 = \left(\frac{1}{A_{\text{chip,srf}} q_{\text{chip}}} U_{T_{\text{sat}}} \right)^2 + \left(\frac{-1}{A_{\text{chip,srf}} q_{\text{chip}}} U_{T_{\text{air}}} \right)^2 + \left[-\frac{T_{\text{sat}} - T_{\text{air}}}{(A_{\text{chip,srf}} q_{\text{chip}})^2} U_{A_{\text{chip,srf}} q_{\text{chip}}} \right]^2 \quad (\text{B17})$$

The uncertainty in the total thermal resistance R_{sys} can be estimated as following.

$$U_{R_{\text{sys}}}^2 = U_{R_{\text{cont}}}^2 + U_{R_{\text{TP}}}^2 + U_{R_{\text{boil}}}^2 + U_{R_{\text{cond}}}^2 \quad (\text{B18})$$

The above uncertainty is shown with the vertical bars appended to symbols in Figs. 7 and 9. As shown in Figs. 7 and 9, the uncertainty in R_{sys} is significantly large at heat fluxes below 100 kWm⁻².

ACKNOWLEDGEMENTS

This research was partially supported by a grant JSPS KAKENHI 15H06301.

REFERENCES

- [1] D.E. Wroblewski, Y. Joshi, Computations of liquid immersion cooling for a protruding heat source in a cubical enclosure, *Int. J. Heat Mass Transf.*, 36 (5) (1993) 1201-1218.
- [2] M.S. El-Genk, H. Bostanci, Saturation boiling of HFE-7100 from a copper surface, simulating a microelectronic chip, *Int. J. Heat Mass Transf.* 46 (2003) 1841–1854.
- [3] P.E. Tuma, The merits of open bath immersion cooling of datacom equipment, *Semiconductor Thermal Measurement and Management Symposium*, 2010. SEMI-THERM 2010. 26th Annual IEEE. IEEE, Santa Clara, CA, Feb. 21-25, (2010).
- [4] F. Agostini, B. Agostini, Flexible two-phase thermosyphon for power electronic cooling, 2011 IEEE 33rd International Telecommunications Energy Conference (INTELEC), (2014), 224-229.
- [5] R. Khodabandeh, B. Palm, Influence of system pressure on the boiling heat transfer coefficient in a closed two-phase thermosyphon loop, *Int. J. Therm. Sci.* 41 (2002) 619–624.
- [6] B., Palm, R. Khodabandeh, Choosing Working Fluid for Two-Phase Thermosyphon Systems for Cooling of Electronics, *ASME. J. Electron. Packag.*, 125(2) (2003) 276-281.
- [7] G. Moreno, S. Narumanchi, C. King, Pool Boiling Heat Transfer Characteristics of HFO-1234yf on Plain and Microporous-Enhanced Surfaces, *J. Heat Transfer.* 135 (2013) 111014. .
- [8] G. Moreno, J.R. Jeffers, S. Narumanchi, Effects of Pressure and a Microporous Coating on HFC-245fa Pool Boiling Heat Transfer, *J. Heat Transfer.* 136 (2014) 101502.
- [9] M.S. El-Genk, A.F. Ali, Enhanced nucleate boiling on copper micro-porous surfaces, *Int. J. Multiph. Flow.* 36 (2010) 780–792. doi:10.1016/j.ijmultiphaseflow.2010.06.003.
- [10] K.N. Rainey, S.M. You, Pool Boiling Heat Transfer From Plain and Microporous, Square Pin-Finned Surfaces in Saturated FC-72, *J. Heat Transfer.* 122 (2000) 509. doi:10.1115/1.1288708.
- [11] Y. Takata, S. Hidaka, M. Masuda, T. Ito, Pool boiling on a superhydrophilic surface, *Int. J. Energy Res.* 27 (2003) 111–119.
- [12] E. Forrest, E. Williamson, J. Buongiorno, L.W. Hu, M. Rubner, R. Cohen, Augmentation of nucleate boiling heat transfer and critical heat flux using nanoparticle thin-film coatings, *Int. J. Heat Mass Transf.* 53 (2010) 58–67. doi:10.1016/j.ijheatmasstransfer.2009.10.008.
- [13] H.T. Phan, N. Caney, P. Marty, S. Colasson, J. Gavillet, Surface wettability control by nanocoating: The effects on pool boiling heat transfer and nucleation mechanism, *Int. J. Heat Mass Transf.* 52 (2009) 5459–5471.
- [14] H. O’Hanley, C. Coyle, J. Buongiorno, T. McKrell, L.-W. Hu, M. Rubner, R. Cohen, Separate effects of surface roughness, wettability, and porosity on the boiling critical heat flux, *Appl. Phys. Lett.* 103 (2013) 24102. doi:10.1063/1.4813450.
- [15] A.Y. Vorobyev, C. Guo, Water sprints uphill on glass, *J. Appl. Phys.* 108 (2010) 123512. doi:10.1063/1.3511431.
- [16] F. Chen, D. Zhang, Q. Yang, J. Yong, G. Du, J. Si, F. Yun, X. Hou, Bioinspired wetting surface via laser microfabrication, *ACS Appl. Mater. Interfaces.* 5 (2013) 6777–6792. doi:10.1021/am401677
- [17] E.W. Lemmon, M.L. Huber, M.O. McLinden, Reference Fluid Thermodynamics and Transport Properties – REFPROP Ver. 9.1, National Institute of Standards and Technology, Boulder, CO, USA (2013).
- [18] G. Myhre, D. Shindell, F.-M. Bréon, W. Collins, J. Fuglestedt, J. Huang, D. Koch, J.-F. Lamarque, D. Lee, B.

- Mendoza, T. Nakajima, A. Robock, G. Stephens, T. Takemura, H. Zhan, 2013: Anthropogenic and Natural Radiative Forcing, in: *Clim. Chang. 2013 Phys. Sci. Basis. Contrib. Work. Gr. I to Fifth Assess. Rep. Intergov. Panel Clim. Chang.*, 2013. doi:10.1017/CBO9781107415324.018.
- [19] M. Hans, F. Müller, S. Grandthyll, S. Hüfner, F. Mücklich, Anisotropic wetting of copper alloys induced by one-step laser micro-patterning, *Appl. Surf. Sci.* 263 (2012) 416–422.
- [20] D. V. Ta, A. Dunn, T.J. Wasley, R.W. Kay, J. Stringer, P.J. Smith, C. Connaughton, J.D. Shephard, Nanosecond laser textured superhydrophobic metallic surfaces and their chemical sensing applications, *Appl. Surf. Sci.* 357 (2015) 248–254. doi:10.1016/j.apsusc.2015.09.027.
- [21] C. Lee, H. Cho, D. Kim, W. Hwang, Fabrication of patterned surfaces that exhibit variable wettability ranging from superhydrophobicity to high hydrophilicity by laser irradiation, *Appl. Surf. Sci.* 288 (2014) 619–624.
- [22] Y.C. Guan, F.F. Luo, G.C. Lim, M.H. Hong, H.Y. Zheng, B. Qi, Fabrication of metallic surfaces with long-term superhydrophilic property using one-stop laser method, *Mater. Des.* 78 (2015) 19–24. doi:10.1016/j.matdes.2015.04.021.
- [23] Y. Vorobyev, C. Guo, Laser turns silicon superwicking, *Opt. Express.* 18 (2010) 6455.
- [24] T.E. Tsai, H.H. Wu, C.C. Chang, S.L. Chen, Two-phase closed thermosiphon vapor-chamber system for electronic cooling, *Int. Commun. Heat Mass Transf.* 37 (2010) 484–489. doi:10.1016/j.icheatmasstransfer.2010.01.010.
- [25] P. Zhang, B. Wang, W. Shi, L. Han, X. Li, Modeling and performance analysis of a two-phase thermosiphon loop with partially/fully liquid-filled downcomer, *Int. J. Refrig.* 58 (2015) 172–185. doi:10.1016/j.ijrefrig.2015.06.014.
- [26] J.R. Taylor, *An Introduction to Error Analysis: The Study of Uncertainties in Physical Measurements*, Mill Valley, CA : University Science Books, (1982)
- [27] R.J. Moffat, Describing the uncertainties in experimental results. *Exp. Therm. Fluid Sci.* 1 (1) (1988) 3-17
- [28] K. Furusato, H. He, M. Yamada, S. Hidaka, M. Kohno, A. Takahashi, Y. Takata, A looped thermosiphon with hydrophobic spots in the evaporator, *Proc. JSME Kyushu annual conf. in Nagasaki*, (2015) 815-3.
- [29] M. Stephan, K., Abdelsalam, Heat-Transfer Correlations for Natural Convection Boiling, *Int. J. Heat Mass Transf.*, 23, (1980) 73-87.
- [30] S.G. Kandlikar, A Theoretical Model to Predict Pool Boiling CHF Incorporating Effects of Contact Angle and Orientation, *J. Heat Transfer.* 123 (2001) 1071. doi:10.1115/1.1409265.
- [31] N. Zuber, *Hydrodynamic Aspects of Boiling Heat Transfer*, Ph.D. thesis, Research Laboratory, Los Angeles and Ramo-Wooldridge Corporation, University of California, Los Angeles, CA (1959).
- [32] M. Zupančič, M. Steinbücher, P. Gregorčič, I. Golobič, Enhanced pool-boiling heat transfer on laser-made hydrophobic/superhydrophilic polydimethylsiloxane-silica patterned surfaces, *Appl. Therm. Eng.* 91 (2015) 288–297. doi:10.1016/j.applthermaleng.2015.08.026.
- [33] S.J. Thiagarajan, R. Yang, C. King, S. Narumanchi, Bubble dynamics and nucleate pool boiling heat transfer on microporous copper surfaces, *Int. J. Heat Mass Transf.* 89 (2015) 1297–1315.
- [34] J.Y. Chang, S.M. You, Enhanced boiling heat transfer from microporous surfaces: effects of a coating composition and method, *Int. J. Heat Mass Transf.* 40 (1997) 4449–4460. doi:10.1016/S0017-9310(97)00057-4.
- [35] M.M. Rahman, E. Ölçeroğlu, M. McCarthy, Role of Wickability on the Critical Heat Flux of Structured Superhydrophilic Surfaces, *Langmuir.* 30 (2014) 11225–11234. doi:10.1021/la5030923.